A coupled BEM/Scaled boundary FEM formulation for accurate computations in linear elastic fracture mechanics

G.E. Bird, J. Trevelyan, C.E. Augarde
Durham University, School of Engineering, South Road, Durham DH1 3LE, UK
Email: g.e.bird@durham.ac.uk, jon.trevelyan@durham.ac.uk, charles.augarde@durham.ac.uk

1 Abstract

Issues relating to the practical implementation of the coupled boundary element-scaled boundary finite element method are addressed in this paper. A detailed approach highlights fully the process of applying boundary conditions, including the treatment of examples in which the assumptions made in previous work are no longer valid. Verification of the method is undertaken by means of estimating stress intensity factors and comparing them against analytical solutions. The coupled algorithm shows good convergence properties. Issues relating to traction scaling, the use of discontinuous boundary elements, and the greater versatility of the coupled method over its constituent methods are highlighted.

Keywords: boundary element method; scaled boundary finite element method; fracture; linear elasticity; coupled methods

2 Introduction

The estimation of stress intensity factors (SIFs) is of fundamental importance in damage tolerance assessment and the prediction of crack propagation in engineering materials. Methods existing to calculate analytically the SIFs are limited to simple geometries. As a result, numerous numerical methods have been developed, each with distinct and overlapping advantages and disadvantages, including the finite element method (FEM), the boundary element method (BEM), the scaled boundary finite element method (SBFEM) [1], the dual boundary element method (DBEM) [2] and the eXtended finite element method (XFEM) [3].

For example, the FEM is known for its ease of implementation; the BEM, DBEM and SBFEM share common advantages of reducing the spatial discretisation dimension by one; and XFEM overcomes many of the remeshing requirements of a more traditional FEM-based crack propagation algorithm. However, their drawbacks include the needs of both the FEM and BEM for a heavily refined mesh in the region of a crack tip, the computation of hypersingular integrals in the DBEM, and the accurate maintenance of a numerical definition of a propagating crack path in XFEM. In efforts to combine their respective advantages, many coupled methods have been published.

The coupled BE-SBFEM combines the geometric flexibility of the BEM to model sections of a domain that may not be simple in nature, with the accuracy of the SBFEM to model the region around a crack tip.

The historical development of the BEM is well-known and is not covered here. The SBFEM is less well-known and its inclusion in coupled methods is summarised here. The SBFEM was predated by the infinitesimal finite-element cell method of Wolf and Song [4] and later the consistent infinitesimal finite-element cell method [5, 6], although all are evolutions of the same method. However, the mathematics behind the original 'mechanically-based' derivation of the SBFEM in the publications of Song and Wolf, may have contributed to its slow uptake by other engineering researchers.

In an effort to raise its awareness and demonstrate its versatility as a tool for computing the dynamic stiffness of an unbounded domain, Song and Wolf re-derived the SBFEM by means of a weighted residual approach, as a displacement formulation in the frequency domain for general problems in elastodynamics in three dimensions [7]. The inclusion of body loads was then addressed and derivations summarised for the SBFEM in two and three dimensions for bounded and unbounded domains [8]. Two 'primer papers' were published to illustrate the SBFEM derived in these two manners along with a worked example [9, 10].

A third (virtual work-based) derivation was presented in Deeks and Wolf [1] alongside a comparable virtual work-based FEM derivation, highlighting their similarities and increasing the accessibility to researchers with a background in solid mechanics. Side face loads and axisymmetric modelling were also addressed and the use of domain substructuring and multiple scaling centres was introduced. Deeks and Wolf then developed a stress recovery technique and a Zienkiewicz-Zhu-based error estimator that provided a direct comparison with the FEM for the first time [11]. The SBFEM was compared favourably with the FEM in applications involving singularities, discontinuities or unbounded domains. This stress recovery technique and error estimator was used in conjunction with an *h*-hierarchical procedure to develop a simple *h*-adaptive mesh refinement strategy [12]. Vu and Deeks later developed a *p*-adaptive refinement procedure and showed that higher order shape functions in this adaptive technique offered improved convergence over *h*-adaptive methods [13, 14]. Deeks developed a method of prescribing Dirichlet boundary conditions (displacement constraints) along side faces [15] and also demonstrated that the use of linear elements can give higher-order results on the undiscretised side faces.

Unlike conventional numerical approaches that, with few exceptions, use a piecewise polynomial basis in which to seek a solution, the SBFEM uses an analytical assumption in the radial direction from its origin. By defining the origin, or *scaling centre*, at a crack tip, the SBFEM has been found effective in the accurate estimation of SIFs. Chidgzey and Deeks [16] showed how the SBFEM can form a truncated series expansion around a scaling centre placed at a crack tip that closely resembles the Williams expansion [17] for determining stress intensity factors in linear elastic fracture mechanics. This allowed for a direct extraction of Williams expansion coefficients from the SBFEM solution. Yang developed an algorithm for automatic modelling of crack propagation through a SBFEM domain [18], and a procedure for fully automated modelling of mixed-mode crack propagation [19]. By introducing a method of substructuring around the crack tip, remeshing complications often associated with crack propagation in other numerical methods were reduced. This procedure was also applied in coupling SBFEM subdomains in the proximity of the crack tip with the FEM in the far field region [20]. Deeks and Augarde also demonstrated the coupling of the SBFEM to a meshless method [21].

An approach similar to Yang [19] is presented here, but with additional motivation. The SBFEM is used to model the singular behaviour of the stress fields around the crack tip by means of a relatively small SBFEM subdomain in the proximity of the crack tip. The far field may contain geometric features for which the SBFEM may not be suited to model, so it is modelled by a relatively large subdomain using the more geometrically flexible BEM. This approach was first demonstrated by Chidgzey *et al.* [22], although results were limited to empirical comparisons. Assumptions were made that limit the application of their scheme to certain sets of boundary conditions. This restriction has been removed in the current paper, and results are compared against analytical solutions. An example of modelling a non-trivial domain is also included in this paper to demonstrate the method's suitability for industrial engineering problems.

Though not presented here, this method forms the basis of work to include the use of DBEM for an efficient BEM mesh and reanalysis [23, 24], where the reuse of data common to multiple analyses lends itself to an efficient BEM-based method of crack propagation prediction. In this approach, the computational efficiency may be enhanced by the reuse of the entire SBFEM matrix if this region is simply translated spatially from one crack growth increment to the next.

3 Numerical formulation of the method

3.1 SBFEM overview

For details of the formulation of the SBFEM the reader is directed to [1]. The key points are summarised here. The *scaled boundary* coordinate system is given by a geometrically-specific coordinate s acting in the circumferential direction running parallel to the boundary, scaled about a geometric *scaling centre* $(\hat{x},\hat{y})$, by a radial coordinate ξ defined by $\xi = 0$ at $(\hat{x},\hat{y})$, that passes through the boundary at $\xi = 1$, as shown in Figure 1(a). The model is discretised in s, but remains analytical in ξ such that displacement of node k in direction $i = x, y$ is defined by the semi-analytical function $u_{ik}(\xi, s)$. As the ξ- and *s*-directions are orthogonal, should the scaling centre be placed on the boundary, there will be two sections of boundary over which s remains constant in the ξ-direction. In such cases, s will become an open axis. The remaining sections of scaled boundary are modelled by *side faces* $\mathrm{A_L}$ and $\mathrm{A_R}$, and do not form part of the discretised boundary, as shown in Figure 1(b). Side faces are a useful property of the SBFEM [16] as they allow the undiscretised analysis of sections of boundary, unlike comparable methods such as the FEM.

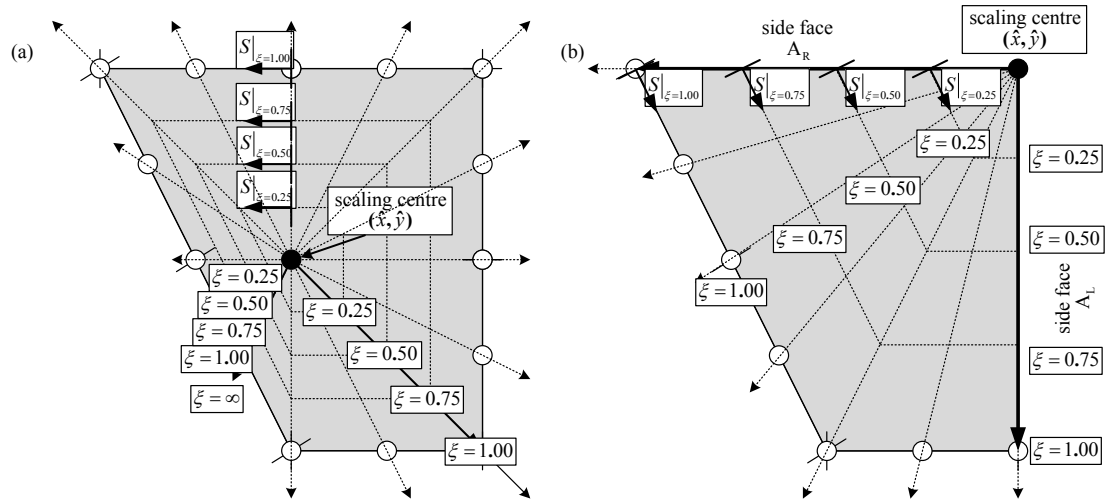

Figure 1. A bounded domain (shaded) modelled using the SBFEM (a) with an internal scaling centre and (b) with the introduction of side faces due to the scaling centre on the boundary

In 2D, the displacement of any point within the domain Ω is considered a linear combination of $2n$ displacement mode shapes, where n is the number of nodes in the model that contribute to its $2n$ degrees of freedom. For each SBFEM model, there is a total of $4n$ mode shapes, since the SBFEM can be used to model both bounded and unbounded (infinite) domains, each requiring a different set of $2n$ mode shapes.

The $4n$ mode shapes are described by a modal displacement matrix $\mathbf{\Phi}$ and a modal force matrix $\mathbf{Q}$, from which subsets $\mathbf{\Phi}_d$ and $\mathbf{Q}_d$, each containing information relating to the $2n$ mode shapes, are selected according to whether the domain is bounded or unbounded. $\mathbf{\Phi}_d$ and $\mathbf{Q}_d$ comprise $2n$ column vectors of $\boldsymbol{\varphi}_j$ and $\mathbf{q}_j$ respectively, such that mode $j = 1...2n$ is defined by $\mathbf{q}_j$, the vector of $2n$ nodal force coefficients required at the boundary to cause displacements given by the corresponding $2n$ nodal displacement coefficients in vector $\boldsymbol{\varphi}_j$. Mode j contributes to the overall displacement by a modal participation factor c_j. The displacement solution $u_{ik}(\xi)$ takes the form

$$u_{ik}(\xi) = \sum_{j=1}^{2n} c_j \xi^{-\lambda_j} \boldsymbol{\varphi}_j \tag{1}$$

where λ_j is the corresponding component of vector $\boldsymbol{\lambda}$, found by the solution of the following $4n \times 4n$ eigenvalue problem

$$\begin{bmatrix} \mathbf{E}_0^{-1}\mathbf{E}_1^{\mathrm{T}} & -\mathbf{E}_0^{-1} \\ \mathbf{E}_1\mathbf{E}_0^{-1}\mathbf{E}_1^{\mathrm{T}} - \mathbf{E}_2 & -\mathbf{E}_1\mathbf{E}_0^{-1} \end{bmatrix} \begin{Bmatrix} \boldsymbol{\varphi}_j \\ \mathbf{q}_j \end{Bmatrix} = \lambda_j \begin{Bmatrix} \boldsymbol{\varphi} \\ \mathbf{q} \end{Bmatrix} \tag{2}$$

Matrices $\mathbf{E}_0$, $\mathbf{E}_1$ and $\mathbf{E}_2$ are found using Green's theorem to evaluate a virtual work expression transformed into the scaled boundary coordinate system, and are given by

$$\mathbf{E}_0 = \int_S \mathbf{B}_1(s)^{\mathrm{T}} \mathbf{D} \mathbf{B}_1(s) \left|\mathbf{J}(s)\right| \mathrm{d}s \tag{3}$$

$$\mathbf{E}_1 = \int_S \mathbf{B}_2(s)^{\mathrm{T}} \mathbf{D} \mathbf{B}_1(s) \left|\mathbf{J}(s)\right| \mathrm{d}s \tag{4}$$

$$\mathbf{E}_2 = \int_S \mathbf{B}_2(s)^{\mathrm{T}} \mathbf{D} \mathbf{B}_2(s) \left|\mathbf{J}(s)\right| \mathrm{d}s \tag{5}$$

Readers will recognise the form of equations (3), (4) and (5) as echoing the expression for evaluating finite element stiffness matrices. In a similar way to this FEM theory, matrices $\mathbf{B}_1$ and $\mathbf{B}_2$ are related to the polynomial shape functions, $\mathbf{D}$ is the constitutive matrix and $\mathbf{J}$ is the Jacobian. The vector of $2n$ modal participation factors $\mathbf{c}$ is given by

$$\mathbf{c} = \boldsymbol{\Phi}_d^{-1} \mathbf{u} \tag{6}$$

where $\mathbf{u}$ is the vector of $2n$ nodal displacements on the boundary. The equivalent forces required to cause these boundary displacements are

$$\mathbf{P} = \mathbf{Q}_d \mathbf{c} = \mathbf{Q}_d \boldsymbol{\Phi}_d^{-1} \mathbf{u} \tag{7}$$

thus it follows the stiffness matrix is given by

$$\mathbf{K} = \mathbf{Q}_d \boldsymbol{\Phi}_d^{-1} \tag{8}$$

so that

$$\mathbf{K}\mathbf{u} = \mathbf{P} \tag{9}$$

Unlike in the conventional FEM, the system of equations governing the SBFEM, and its construction, comprises boundary nodal displacements and forces only, without the need for volumetric discretisation, or discretisation of some sections of boundary (side faces). However, it should be noted that the solution of equation (2) is computationally inefficient as in finding the bounded domain mode shapes, for example, the unbounded domain mode shapes are found as a by-product, when perhaps just one case is of interest.

The SBFEM suffers also from a 'line of sight' meshing requirement [1] that limits its applicability. Though this can be overcome by substructuring the domain into multiple SBFEM subdomains [15], this can still prove awkward when meshing domains that would be modelled by the BEM or FEM with relative ease. This is one of the principal motivating factors for the current work.

3.2 Coupled BE-SBFEM

The following overview of the coupled BE-SBFEM briefly describes its formulation and assumes some prior knowledge of its constituent methods. Throughout the derivation, subscripts B and S are used to denote the BEM and SBFEM subdomains respectively, separated by a common interface denoted by subscript I. For simplicity, the derivation focuses on the coupling of two subdomains in two dimensions such as in Figure 2, where a domain Ω is divided into a BEM subdomain Ω_{B} and a SBFEM subdomain Ω_{S} bounded by Γ_{B} and Γ_{S} respectively, and separated by a common interface Γ_{I}. The additional subscript J denotes *junction* degrees of freedom, i.e. those associated with the nodes found at the junction of the boundaries Γ_{B}, Γ_{S} and Γ_{I}. The two junction nodes are denoted J1 and J2, as illustrated in Figure 2. In the illustrated example, Γ_{B} includes use of discontinuous boundary elements in order to highlight later the additional considerations required when using these elements over those necessary when using just continuous boundary elements.

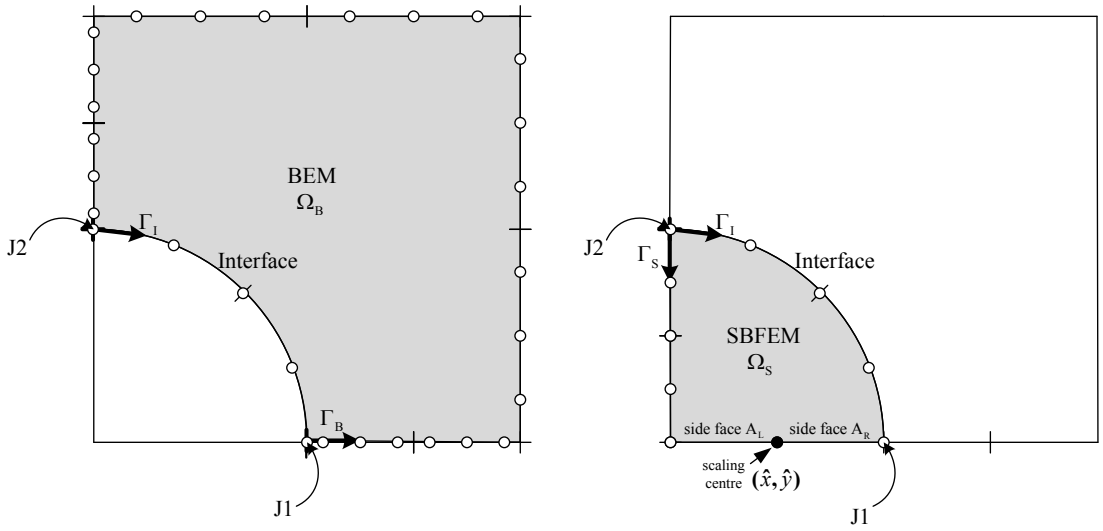

Figure 2. An example domain subdivided into BEM and SBFEM subdomains.

The conventional influence matrices [25] describing Ω_B, can be partitioned into their J, I and B components

$$\begin{bmatrix} \mathbf{H}_{JJ} & \mathbf{H}_{JI} & \mathbf{H}_{JB} \\ \mathbf{H}_{IJ} & \mathbf{H}_{II} & \mathbf{H}_{IB} \\ \mathbf{H}_{BJ} & \mathbf{H}_{BI} & \mathbf{H}_{BB} \end{bmatrix} \begin{Bmatrix} \mathbf{u}_J \\ \mathbf{u}_I \\ \mathbf{u}_B \end{Bmatrix} = \begin{bmatrix} \mathbf{G}_{JJ} & \mathbf{G}_{JI} & \mathbf{G}_{JB} \\ \mathbf{G}_{IJ} & \mathbf{G}_{II} & \mathbf{G}_{IB} \\ \mathbf{G}_{BJ} & \mathbf{G}_{BI} & \mathbf{G}_{BB} \end{bmatrix} \begin{Bmatrix} \mathbf{t}_J \\ \mathbf{t}_I \\ \mathbf{t}_B \end{Bmatrix} \tag{10}$$

Similarly equation (9) describing Ω_S can be partitioned into its J, I and S components

$$\begin{bmatrix} \mathbf{K}_{JJ} & \mathbf{K}_{JI} & \mathbf{K}_{JS} \\ \mathbf{K}_{IJ} & \mathbf{K}_{II} & \mathbf{K}_{IS} \\ \mathbf{K}_{SJ} & \mathbf{K}_{SI} & \mathbf{K}_{SS} \end{bmatrix} \begin{Bmatrix} \mathbf{u}_J \\ \mathbf{u}_I \\ \mathbf{u}_S \end{Bmatrix} = \begin{Bmatrix} \mathbf{P}_J \\ \mathbf{P}_I \\ \mathbf{P}_S \end{Bmatrix} \tag{11}$$

Decomposing the nodal forces on Γ_S, Γ_I and at junction nodes J1 and J2 into their internal and external components

$$\begin{aligned} \mathbf{P}_J &= \mathbf{P}_{Jint} + \mathbf{P}_{Jext} \\ \mathbf{P}_I &= \mathbf{P}_{Iint} + \mathbf{P}_{Iext} \\ \mathbf{P}_S &= \mathbf{P}_{Sint} + \mathbf{P}_{Sext} \end{aligned} \tag{12}$$

The interface is defined *exclusive* of the junction nodes and therefore is entirely internal; thus there are no external forces so

$$\mathbf{P}_{Iext} = \mathbf{0} \tag{13}$$

Similarly, the SBFEM boundary is also defined *exclusive* of the junction nodes and is entirely external (on the boundary); thus there are no internal forces so

$$\mathbf{P}_{Sint} = \mathbf{0} \tag{14}$$

Interface tractions are related to the interface forces by the a traction-force transformation matrix $\mathbf{M}$, described by Becker [25], and decomposed into

$$\begin{bmatrix} \mathbf{M}_{JJ} & \mathbf{M}_{JI} \\ \mathbf{M}_{IJ} & \mathbf{M}_{II} \end{bmatrix} \begin{Bmatrix} \mathbf{t}_J \\ \mathbf{t}_I \end{Bmatrix} = \begin{Bmatrix} -\mathbf{P}_{Jint} \\ -\mathbf{P}_{Iint} \end{Bmatrix} \tag{15}$$

Thus, combining equations (12) and (15) gives

$$\begin{bmatrix} \mathbf{K}_{JJ} & \mathbf{K}_{JI} & \mathbf{K}_{JS} & \mathbf{M}_{JJ} & \mathbf{M}_{JI} \\ \mathbf{K}_{IJ} & \mathbf{K}_{II} & \mathbf{K}_{IS} & \mathbf{M}_{IJ} & \mathbf{M}_{II} \\ \mathbf{K}_{SJ} & \mathbf{K}_{SI} & \mathbf{K}_{SS} & \mathbf{0} & \mathbf{0} \end{bmatrix} \begin{Bmatrix} \mathbf{u}_J \\ \mathbf{u}_I \\ \mathbf{u}_S \\ \mathbf{t}_J \\ \mathbf{t}_I \end{Bmatrix} = \begin{Bmatrix} \mathbf{0} \\ \mathbf{0} \\ \mathbf{P}_{Sint} \end{Bmatrix} + \begin{Bmatrix} \mathbf{P}_{Jext} \\ \mathbf{P}_{Iext} \\ \mathbf{P}_{Sext} \end{Bmatrix} \tag{16}$$

Combining equations (16) with (13) and (14) gives

$$\begin{bmatrix} \mathbf{K}_{JJ} & \mathbf{K}_{JI} & \mathbf{K}_{JS} & \mathbf{M}_{JJ} & \mathbf{M}_{JI} \\ \mathbf{K}_{IJ} & \mathbf{K}_{II} & \mathbf{K}_{IS} & \mathbf{M}_{IJ} & \mathbf{M}_{II} \\ \mathbf{K}_{SJ} & \mathbf{K}_{SI} & \mathbf{K}_{SS} & \mathbf{0} & \mathbf{0} \end{bmatrix} \begin{Bmatrix} \mathbf{u}_J \\ \mathbf{u}_I \\ \mathbf{u}_S \\ \mathbf{t}_J \\ \mathbf{t}_I \end{Bmatrix} = \begin{Bmatrix} \mathbf{P}_{Jext} \\ \mathbf{0} \\ \mathbf{P}_{Sext} \end{Bmatrix} \tag{17}$$

This differs from [22], where J1 and J2 were considered part of the interface, limiting boundary conditions to $\mathbf{P}_{Jext} = \mathbf{0}$. As equation (17) now contains no terms representing internal forces, the 'ext' subscripts are dropped for brevity. Combining equations (10) and (17) provides the coupled system

$$\begin{bmatrix} \mathbf{K}_{JJ} & \mathbf{K}_{JI} & \mathbf{K}_{JS} & \mathbf{M}_{JJ} & \mathbf{M}_{JI} & \mathbf{0} & \mathbf{0} \\ \mathbf{K}_{IJ} & \mathbf{K}_{II} & \mathbf{K}_{IS} & \mathbf{M}_{IJ} & \mathbf{M}_{II} & \mathbf{0} & \mathbf{0} \\ \mathbf{K}_{SJ} & \mathbf{K}_{SI} & \mathbf{K}_{SS} & \mathbf{0} & \mathbf{0} & \mathbf{0} & \mathbf{0} \\ \mathbf{H}_{JJ} & \mathbf{H}_{JI} & \mathbf{0} & -\mathbf{G}_{JJ} & -\mathbf{G}_{JI} & \mathbf{H}_{JB} & -\mathbf{G}_{JB} \\ \mathbf{H}_{IJ} & \mathbf{H}_{II} & \mathbf{0} & -\mathbf{G}_{IJ} & -\mathbf{G}_{II} & \mathbf{H}_{IB} & -\mathbf{G}_{IB} \\ \mathbf{H}_{BJ} & \mathbf{H}_{BI} & \mathbf{0} & -\mathbf{G}_{BJ} & -\mathbf{G}_{BI} & \mathbf{H}_{BB} & -\mathbf{G}_{BB} \end{bmatrix} \begin{Bmatrix} \mathbf{u}_J \\ \mathbf{u}_I \\ \mathbf{u}_S \\ \mathbf{t}_J \\ \mathbf{t}_I \\ \mathbf{u}_B \\ \mathbf{t}_B \end{Bmatrix} = \begin{Bmatrix} \mathbf{P}_J \\ \mathbf{0} \\ \mathbf{P}_S \\ \mathbf{0} \\ \mathbf{0} \\ \mathbf{0} \end{Bmatrix} \tag{18}$$

Boundary conditions are applied, and then by separating known and unknown terms in equation (18) in the usual manner, can be rearranged to yield a square system of linear equations in the form

$$\mathbf{A}\mathbf{x} = \mathbf{b} \tag{19}$$

where $\mathbf{x}$ is the vector of unknown displacements and tractions.

3.3 Matrix scaling

In almost all mechanical problems using typical engineering materials, it is likely that the traction coefficients $\mathbf{t}$ will be several orders of magnitude larger than the displacement coefficients $\mathbf{u}$ when using conventional SI units. By selecting an appropriate value for a scale factor Ψ, and introducing it into the BEM system matrix

$$\mathbf{H}\mathbf{u} = \Psi\mathbf{G}\frac{\mathbf{t}}{\Psi} \tag{20}$$

the displacement and scaled traction influence matrices, $\mathbf{H}$ and $\Psi\mathbf{G}$, are of the same order, improving matrix conditioning. Thus, equation (18) is rewritten

$$\begin{bmatrix} \mathbf{K}_{JJ} & \mathbf{K}_{JI} & \mathbf{K}_{JS} & \Psi\mathbf{M}_{JJ} & \Psi\mathbf{M}_{JI} & \mathbf{0} & \mathbf{0} \\ \mathbf{K}_{IJ} & \mathbf{K}_{II} & \mathbf{K}_{IS} & \Psi\mathbf{M}_{IJ} & \Psi\mathbf{M}_{II} & \mathbf{0} & \mathbf{0} \\ \mathbf{K}_{SJ} & \mathbf{K}_{SI} & \mathbf{K}_{SS} & \mathbf{0} & \mathbf{0} & \mathbf{0} & \mathbf{0} \\ \mathbf{H}_{JJ} & \mathbf{H}_{JI} & \mathbf{0} & -\Psi\mathbf{G}_{JJ} & -\Psi\mathbf{G}_{JI} & \mathbf{H}_{JB} & -\Psi\mathbf{G}_{JB} \\ \mathbf{H}_{IJ} & \mathbf{H}_{II} & \mathbf{0} & -\Psi\mathbf{G}_{IJ} & -\Psi\mathbf{G}_{II} & \mathbf{H}_{IB} & -\Psi\mathbf{G}_{IB} \\ \mathbf{H}_{BJ} & \mathbf{H}_{BI} & \mathbf{0} & -\Psi\mathbf{G}_{BJ} & -\Psi\mathbf{G}_{BI} & \mathbf{H}_{BB} & -\Psi\mathbf{G}_{BB} \end{bmatrix} \begin{Bmatrix} \mathbf{u}_J \\ \mathbf{u}_I \\ \mathbf{u}_S \\ \frac{\mathbf{t}_J}{\Psi} \\ \frac{\mathbf{t}_I}{\Psi} \\ \mathbf{u}_B \\ \frac{\mathbf{t}_B}{\Psi} \end{Bmatrix} = \begin{Bmatrix} \mathbf{P}_J \\ \mathbf{0} \\ \mathbf{P}_S \\ \mathbf{0} \\ \mathbf{0} \\ \mathbf{0} \end{Bmatrix} \tag{21}$$

and by the application of boundary conditions reduces once more to equation (19), but now $\mathbf{x}$ is the vector of unknown displacements and *scaled* tractions. The effect of Ψ is to improve the condition number of the system matrix. An optimum value for Ψ may not be known *a priori*, but an appropriate value can be based on the Young's modulus and the size and type of the domain under analysis.

3.4 Additional BEM considerations

The SBFEM requires Γ_S be meshed using continuous elements. Consequently, the interface Γ_I must be meshed using continuous elements in order to provide a fully continuous SBFEM subdomain boundary. However, the BEM boundary Γ_B can be meshed using either continuous or discontinuous elements, or some combination of the two types. Thus, consideration must be made when using discontinuous boundary elements within the coupled BE-SBFEM.

Collocation using the BEM requires the use of singular integration routines to evaluate singular integrals when integrating over the section of boundary (element) on which the collocation point lies. At both J1 and J2 there are junctions between the discontinuous elements on the boundary and the continuous elements on the interface. It should be noted that when collocating at J1 and J2 and integrating over the adjacent element on Γ_B, if the element is of the discontinuous type, a singular integration scheme is required [26], even though the node does not contribute to the set of nodes defining the element geometry.

4 Results

4.1 Analytical verification

4.1.1 Through crack in an infinite plate example 1

A BE-SBFEM model of dimensions $b \times h$ is defined in the immediate vicinity of the tip of a crack of length $2a$ central to an infinite plate subject to a uniaxial load of σ, such that the section of crack face modelled is of length $\bar{a}$, and the crack tip is coincident with the SBFEM scaling centre $(\hat{x}, \hat{y})$, as shown in Figure 3.

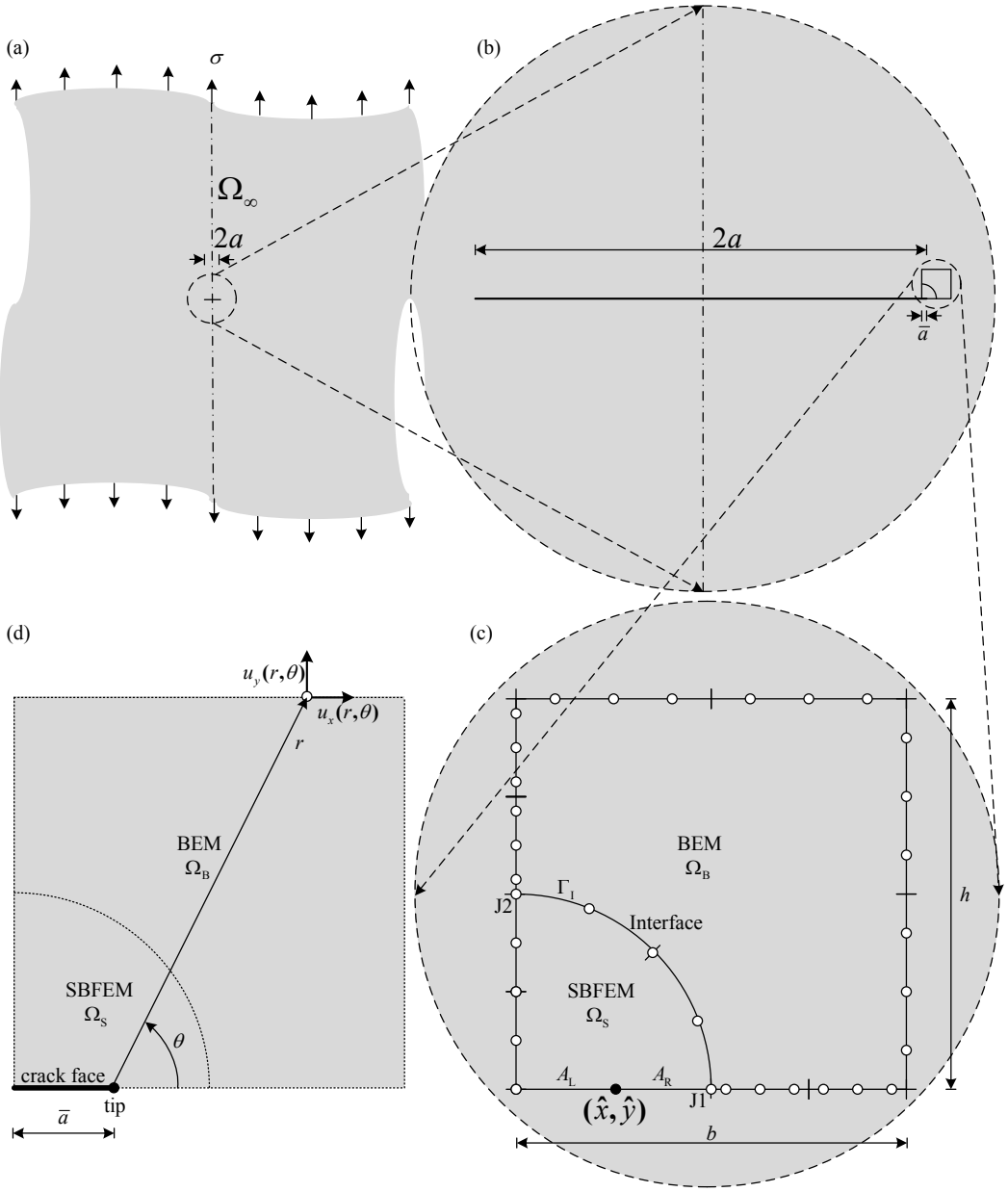

Figure 3. (a) Through crack in an infinite plate, (b) the section of the crack that is modelled, (c) the BE-SBFEM model of the immediate vicinity of the crack tip and (d) the Williams expansion coordinate system [17], used in the approximation of displacements u_x and u_y

As $\bar{a} << a$, the displacements that would occur locally as the result of the load on the infinite plate can be estimated by [27] as

$$u_x(r,\theta) = \frac{K_{\mathrm{I}}^{\mathrm{exact}}}{\mu}\sqrt{\frac{r}{2\pi}}\cos\frac{\theta}{2}\left[\frac{1}{2}(\kappa-1)+\sin^2\frac{\theta}{2}\right] \tag{22}$$

$$u_y(r,\theta) = \frac{K_{\mathrm{I}}^{\mathrm{exact}}}{\mu}\sqrt{\frac{r}{2\pi}}\sin\frac{\theta}{2}\left[\frac{1}{2}(\kappa+1)-\cos^2\frac{\theta}{2}\right] \tag{23}$$

where

$$K_{\mathrm{I}}^{\mathrm{exact}} = \sigma\sqrt{\pi a} \tag{24}$$

A plane stress assumption is made, so

$$\kappa = \frac{3-\nu}{1+\nu} \tag{25}$$

$$\mu = \frac{E}{2(1+\nu)} \tag{26}$$

in which E is the Young's modulus, μ is the shear modulus and ν is the Poisson's ratio of the material. Displacement boundary conditions given by equations (22) and (23) are prescribed on all sections of Γ_B and Γ_S, except where traction-free boundary conditions can be applied, i.e. in the *x*-direction to sections of Γ_B where $\theta = 0$, and side faces A_L and A_R, and junction node J1, and in the *y*-direction to the side face A_L. Other than the assumed continuity between Ω_B and Ω_S, no boundary conditions are applied to Γ_I and its nodal displacements remain as unknowns to be solved. Without loss of generality, the model is meshed with n_e quadratic elements per discretised line on boundaries Γ_B, Γ_S and Γ_I, totalling *n* degrees of freedom in the coupled system, which is solved for unknown nodal tractions and displacements.

The accuracy of the *i*-direction displacement $u_i(\xi, s)$ at some point within Ω_S is dependent on both the accuracy of the nodal displacement $u_i(1, s)$, and the force and displacement modes computed prior to forming the stiffness matrix in equation (8). In this example, the majority of the nodal displacements $u_i(1, s)$ are prescribed as boundary conditions so it would be inappropriate to use them to determine the accuracy of the BE-SBFEM. Instead, values of $u_i(\xi, s)$ are computed according to the boundary coordinates where $u_i(1, s)$ is not prescribed. Regions within Ω_S can be defined whose displacements can be computed without the bias of prescribed boundary conditions, denoted by Ω_{Si} where

$$\Omega_{Si} := (\xi, s), 0 < \xi \le 1, s_{\min} < s < s_{\max}, i = x, y \tag{27}$$

as illustrated by the shaded regions in Figure 4.

Nodal displacements can be extracted directly; non-nodal displacements can be estimated by interpolating nodal displacement values. To maintain high accuracy, sample points are taken along axes of constant s that coincide with the boundary coordinates of the nodes such that this interpolation is not necessary. Interior sample points are defined by the intersection of these axes and the n_b contours (or *scaled boundaries*) sampled within the region, and are illustrated by the example in Figure 4, where $n_b = 8$.

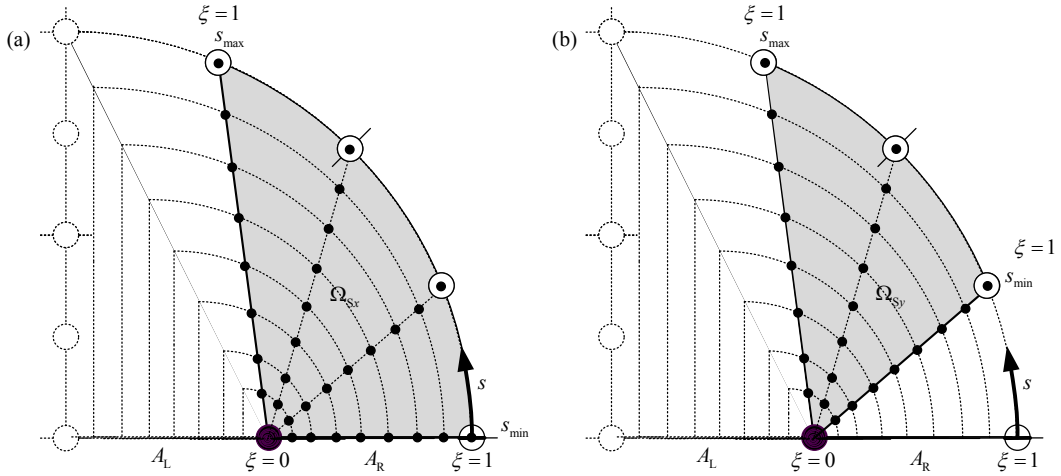

Figure 4. Shaded regions $\Omega_{Sx}(\xi,s)$ and $\Omega_{Sy}(\xi,s)$ within Ω_S where (a) *x*- and (b) *y*-direction displacements respectively at nodes and additional interior sample points (indicated by the black circles) can be used for verification of the accuracy of the BE-SBFEM

The displacement recovered at each sample point within Ω_{Si} is used with equations (22) and (23) to compute $K_I(\xi,s,i)$, an estimation to K_I^{exact}. The percentage error of this estimation is defined by

$$\varepsilon(\xi,s,i) = \left| \frac{K_I(\xi,s,i) - K_I^{\text{exact}}}{K_I^{\text{exact}}} \right| \times 100\% \tag{28}$$

In this example the model properties are $E = 207\text{GPa}$, $\nu = 0.3$, $h = b = 4\text{mm}$, and $A_L = A_R = \bar{a} = 0.001a = 1\text{mm}$, and the applied load is $\sigma = 1\text{MPa}$. The range of model mesh densities is from $n_e = 2$ to $n_e = 10$. Sample contour plots of $\varepsilon(\xi,s,i)$ estimated within the ranges defined in equation (27) are shown in Figure 5.

The convergence of K_I results with n is presented in Figure 6. Results are shown using a family of curves, each considering K_I as derived from BE-SBFEM results obtained using $\xi = \{0.1, 0.3, 0.5, 0.7, 0.9\}$. It should be noted that K_I can be established from the results at any point in Ω_{Si}, and the errors illustrated in Figure 6 are used as an indicator of suitable regions within which to choose such a point.

By increasing n_e, not only does the accuracy at individual points increase, the range $(s_{\max} - s_{\min})$ is extended allowing a greater total number of sample points to be taken within Ω_{Si}. Increasing this range shows that the highest errors occur typically in the region close to $s = 0$. Moreover, it can be seen that the errors are significantly lower in *y*-direction degrees of freedom than those in the *x*-direction. Further, the results do not necessarily exhibit greater accuracy at $\xi = 1$. These observations are significant as [22] use the *x*-direction displacement at $(\xi,s) = (1,0)$ to estimate K_I, where errors are potentially among their highest.

Displacements in this type of problem are dominated by those in the *y*-direction, thus the percentage errors $\varepsilon(\xi, s, y)$ are expected *a priori* to be lower than $\varepsilon(\xi, s, x)$. With this knowledge, a convergence estimate is defined by $\varepsilon(1, s_{\max}, y)$ where errors are predicted to be amongst their lowest. An example of the convergence effect of increasing *n* is shown in Figure 6.

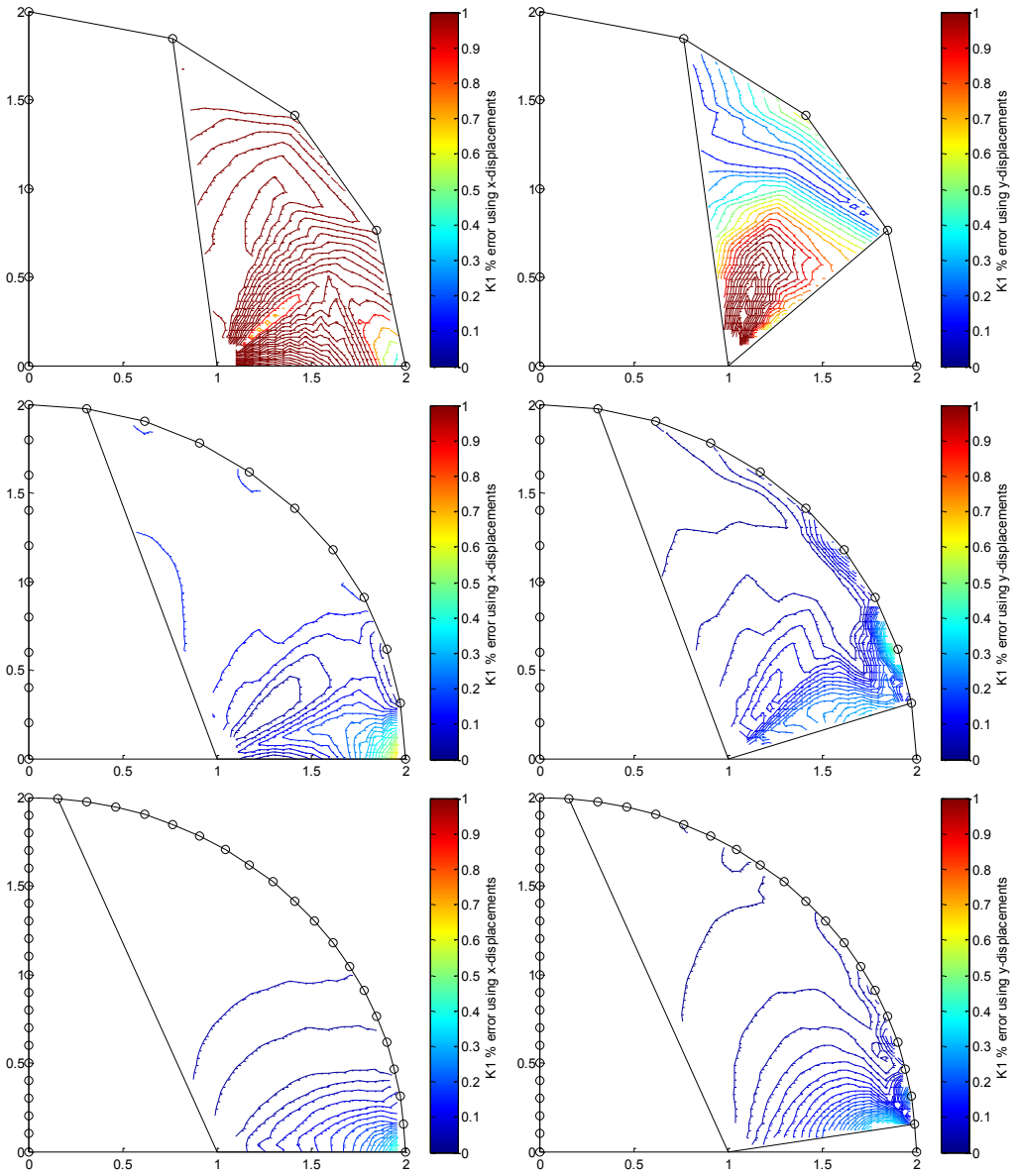

Figure 5. Variation of % errors in K_I within sample domains for (a) n_e=2, (b) n_e=5 and (c) n_e=10

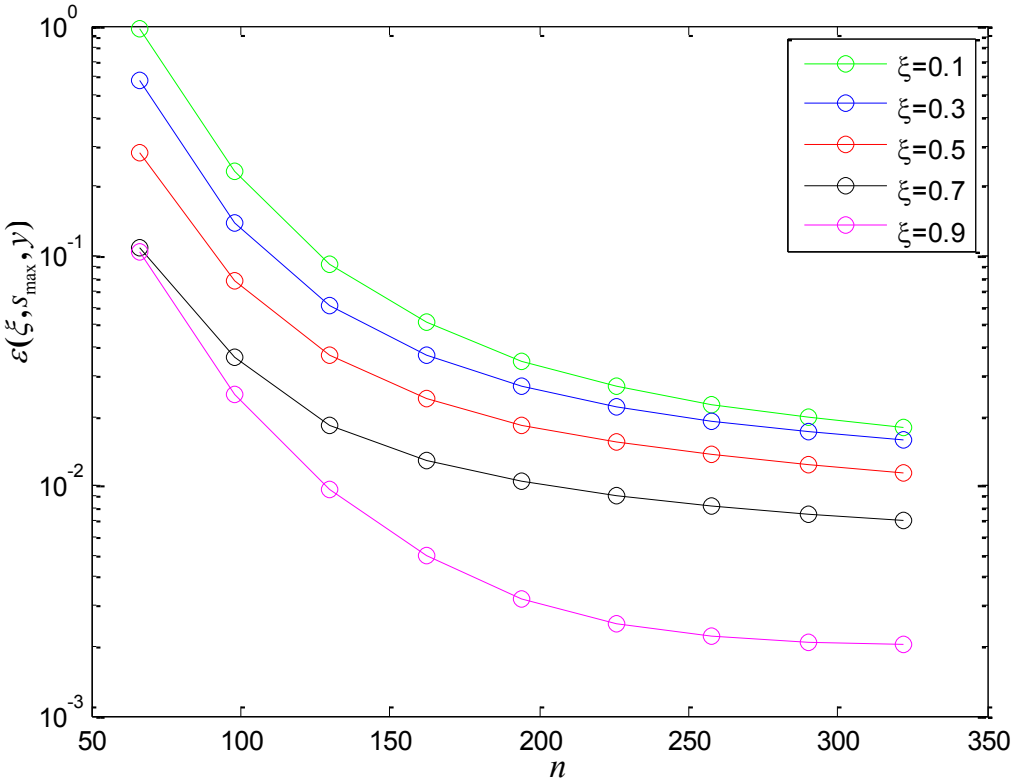

Figure 6. Convergence of error in estimation of K_I with increase in calculated using *y*-direction displacements at $s=s_{max}$

4.1.2 Through crack in an infinite plate example 2

In the previous example, Ω is sufficiently trivial for the SBFEM to model alone. However, one attractive property of the coupled BE-SBFEM is its ability to model complicated geometries under fracture analysis. The choice of geometry around the crack tip used to model $\bar{a}$ in this verification process is arbitrary. The square region of dimensions $h \times b$ may be replaced by a more complicated geometry because the analytical solutions used in both the application of boundary conditions and the comparison of nodal displacement solutions are independent of model geometry. Thus, in the following example, the crack tip region is modelled by Ω_S coupled to a more complicated Ω_B where the same method of comparison to an analytical solution is available.

The model and example results are shown in Figure 7 from which it can be seen that the complexity of the problem has little effect on the convergence characteristics of the method.

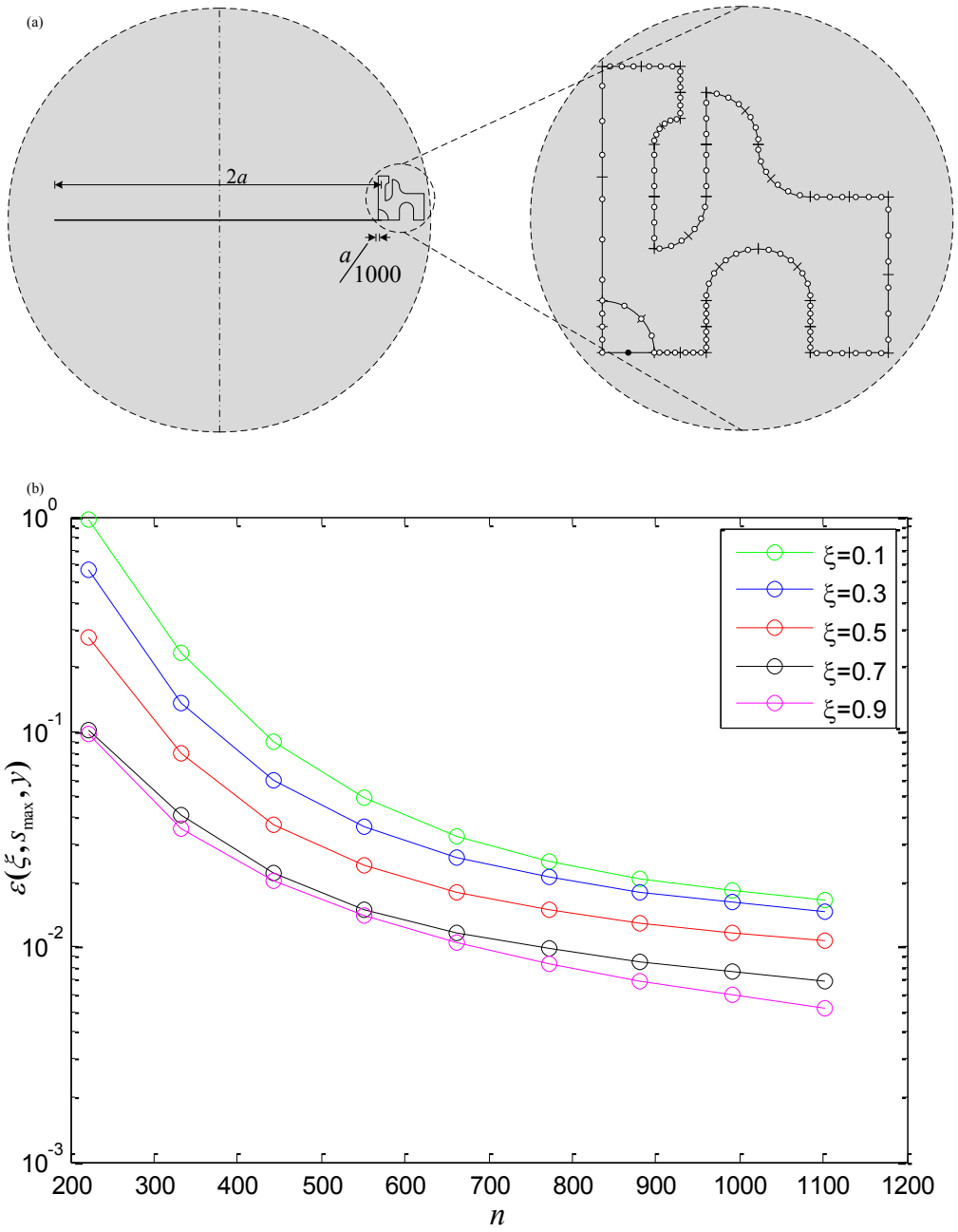

Figure 7. Irregular example with analytical solution highlighting the BE-SBFEM's geometric flexibility. (a) the BEM and SBFEM subdomains around the crack tip, and (b) the convergence of error in estimation of K_I with increase in calculated using *y*-direction displacements at s=s_{max}

4.2 Strategy for estimation of stress intensity factor

The foregoing examples demonstrate that the accuracy to which K_I can be estimated by $K_I(\xi,s,i)$ is dependent upon both the choice of location of the point $(\xi,s)\in\Omega_S$, and also the displacement component at that point, used to determine the estimate using equations (22) and (23). However, the optimal values of these parameters are problem-dependent, so the purpose of the analytical verification is to establish a strategy for the estimation of stress intensity factors for general problems of this nature, for which analytical solutions may not be available.

Based on the analytical verification, this strategy is summarised as using:

- displacements in direction of the predicted maximum displacement ;
- displacements that are of greatest magnitude, i.e. those in the region around the crack opening;
- displacements that are in the immediate vicinity of the crack tip, so that equations (22) and (23) are valid.

4.3 Numerical verification

4.3.1 Through crack in a finite plate

A BE-SBFEM model of dimensions $h \times b$ is used to model a through crack of length $2a$ central to a finite plate of dimensions $2h \times 2b$ with subject to a uniaxial load of σ, as shown in Figure 8. In this example, $E = 210\text{GPa}$ $a = 1\text{mm}$, $a/b = 0.2$ and $h/b = 2$. The units of all values of K_I quoted in the present work are $\text{MPa}\,\text{mm}^{0.5}$.

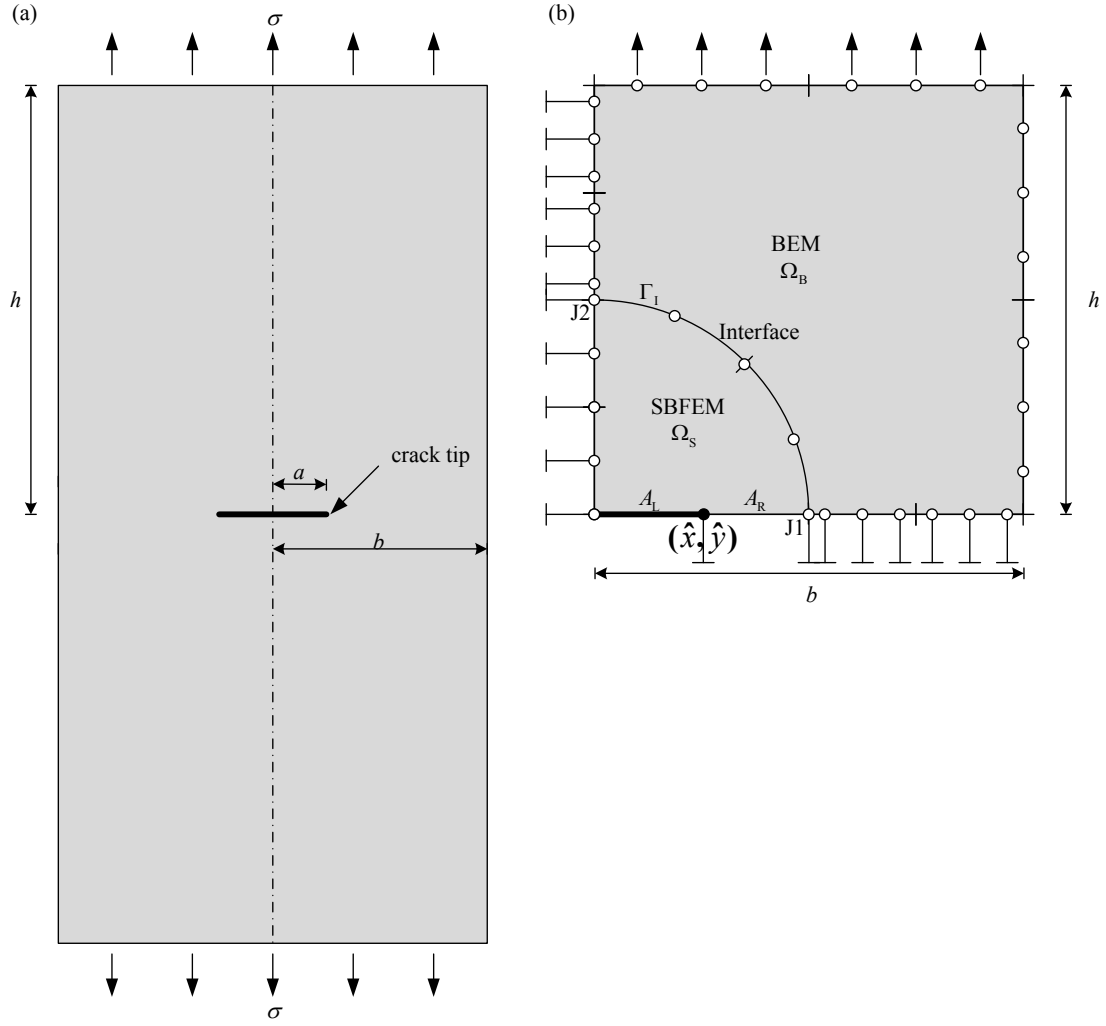

Figure 8. (a) The finite plate with through crack and (b) the BE-SBFEM model

Displacements are recovered that can be used to determine $K_I(\xi, s, i)$, without any *a priori* knowledge of an optimum sample point location for which $\varepsilon(\xi, s, i)$ may be reduced or minimised, other than the general strategy outlined in 4.2. An analytical

reference solution is unavailable for this problem, and stated reference values are presented with insufficient precision for this purpose. However, given the accuracy demonstrated in examples 4.1.1 and 4.1.2, errors are taken relative to the converged solution $\bar{K}_{\mathrm{I}}(\xi,i)$ as, defined by

$$\bar{\varepsilon}(\xi,s,i)=\left|\frac{K_{\mathrm{I}}(\xi,s,i)-\bar{K}_{\mathrm{I}}(\xi,i)}{\bar{K}_{\mathrm{I}}(\xi,i)}\right|\times 100\% \tag{29}$$

Figure 9 shows the converged solution for samples of $\xi=\{0.1,0.3,0.5,0.7,0.9\}\times 10^{-5}$, found using y-direction displacements. In this example, the five converged results range from $\bar{K}_{\mathrm{I}}=3.3294$ to $\bar{K}_{\mathrm{I}}=3.3334$, which compare well with the value of $K_{\mathrm{I}}=3.332$ estimated by Aliabadi [28], achieved using the DBEM in which a reference value of $K_{\mathrm{I}}=3.324$ is cited [29].

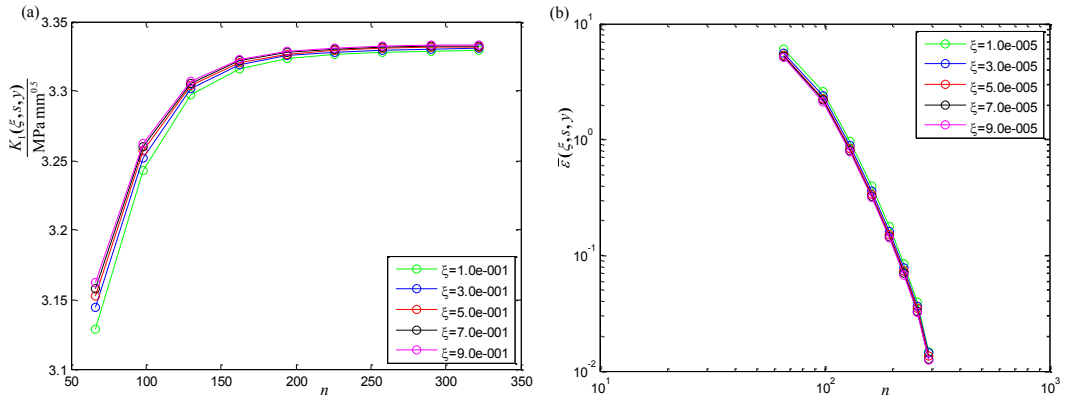

Figure 9. (a) Convergence and (b) convergence rate of % error in estimation of K_{I} for through crack in finite plate

4.3.2 Edge crack in a finite plate

A BE-SBFEM model of dimensions $h\times b$ is used to model an edge crack of length a that has developed symmetrically in a finite plate of dimensions $2h\times b$, subjected to a uniaxial load of σ, as shown in Figure 10. In order to constrain the model fully in the x-direction, a boundary condition of $u_x=0$ is prescribed at one node, as indicated in the figure.

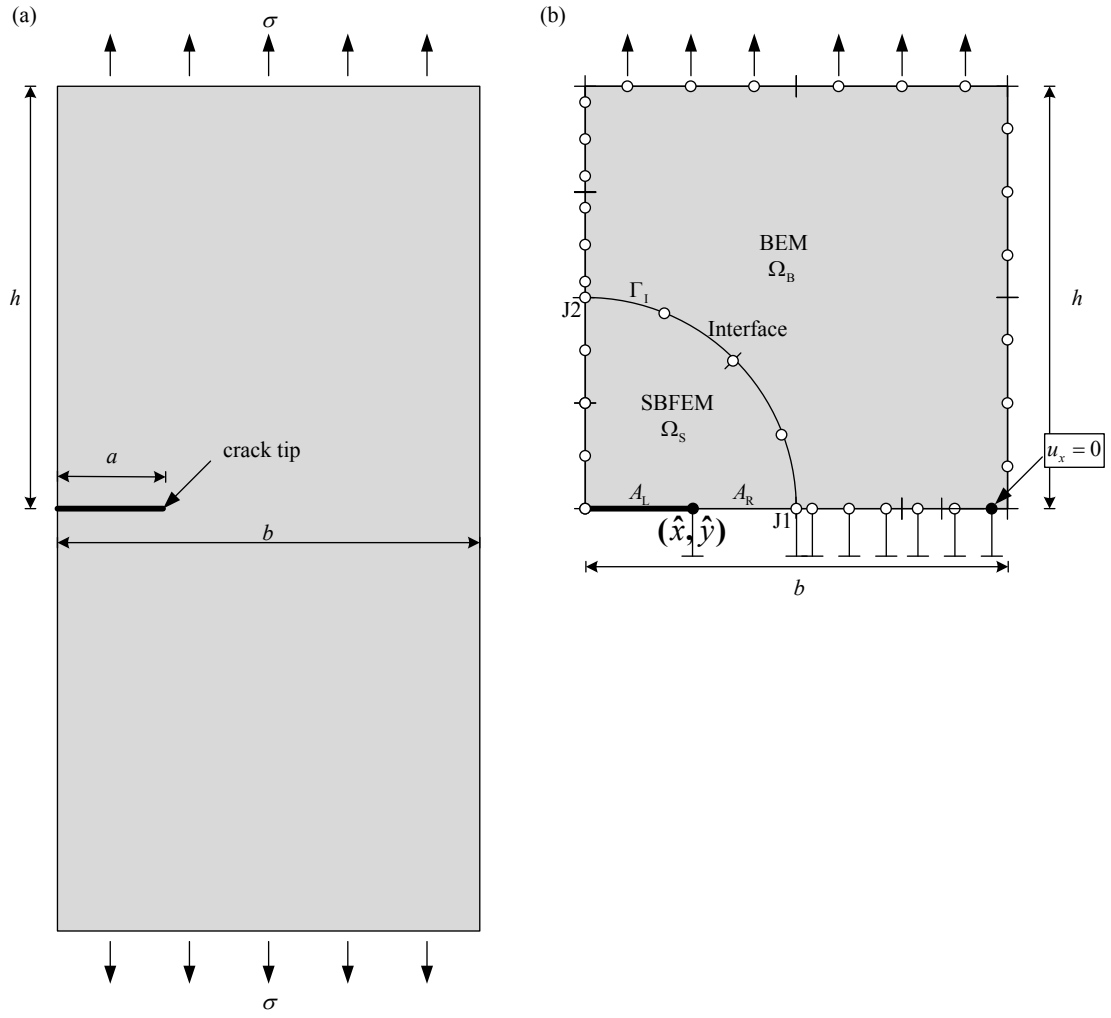

Figure 10. (a) The finite plate with edge crack and (b) the BE-SBFEM model

Following the same strategy as before, errors are indicated by equation (29) as an analytical reference solution for this problem is unavailable, and are summarised in Figure 11. In this example, the five converged results range from $\bar{K}_{\mathrm{I}} = 2.644$ to $\bar{K}_{\mathrm{I}} = 2.645$, which compare favourably with the value of $K_{\mathrm{I}} = 2.66$ estimated by Portela *et al*. [30], achieved using the DBEM in which a reference value of $K_{\mathrm{I}} = 2.64$ is cited [31]. It should also be noted that while convergence was reached by Portela *et al* with $n = 144$, their initial mesh was graded. In the present work, the model is meshed uniformly with convergence (to 2 s.f.) at $n = 130$. Further, because the mesh is refined uniformly, the majority of the additional degrees of freedom appear on Γ_{B}, and as shown in the example in 4.1.2, the distribution of degrees of freedom in Ω_{B} has little contribution to the increase in accuracy with n. Thus, with a graded mesh, the BE-SBFEM solution may converge faster still.

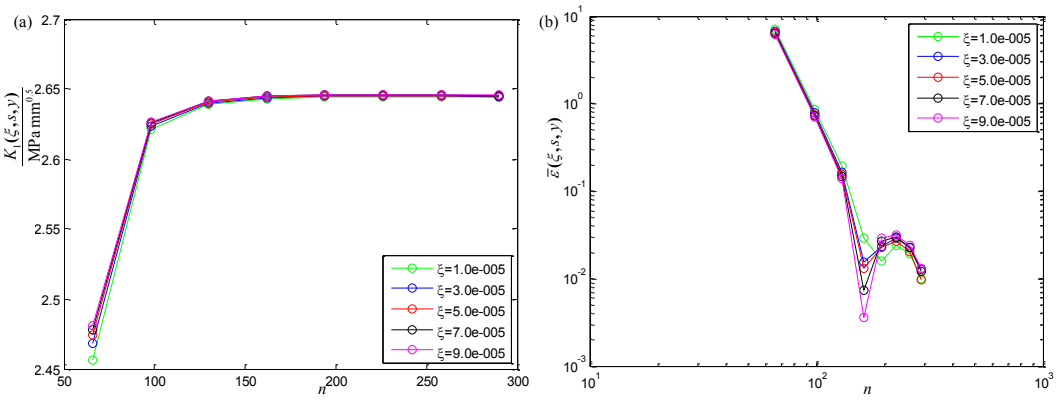

Figure 11. (a) Convergence and (b) convergence rate of % error in estimation of K_I for edge crack in finite plate

4.4 Matrix scaling

The effect of varying the boundary element traction scale factor Ψ described in equation (21) on the condition number of system matrix $\mathbf{A}$ in example 4.1.1 for $n_e = 1$ is illustrated in Figure 12. Though this value may not be an accurate optimum for a minimum condition number, it can be seen that this is not necessary as sufficient reductions can be made simply by the use of a scale factor of a suitable order of magnitude.

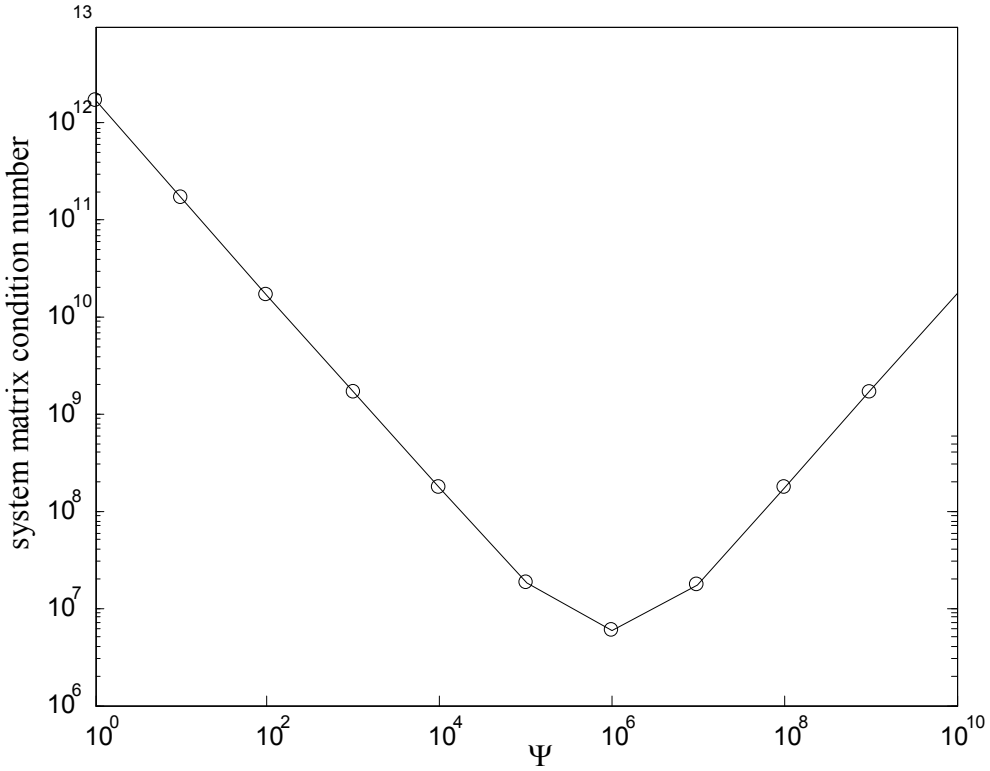

Figure 12. Effect of varying traction scaling parameter on the condition number of the coupled BE-SBFEM system matrix A

All the results published in this paper have been generated using code developed in MATLAB, making use of the 'backslash' operator mldivide†, a function that selects a solver appropriate for the type of system to be solved. Consequently, ill-conditioned systems of the order 10^{13}, such as found by selecting $\Psi = 1$ in both analytical verification examples, were solved to the same level of accuracy as those with $\Psi = 10^6$. However, should the method be written without such solvers, care should be taken to avoid ill-conditioning by selecting an appropriate scaling factor, such that the terms in the influence matrices, $\mathbf{H}$ and $\Psi\mathbf{G}$, are of the same order of magnitude. Analysis of Figure 12, and similar curves produced for different problems of the type analysed in the present work, suggests $\Psi \approx 10^6$ is suitable in all the examined cases. Thus, for all examples considered in the present work a scale factor of $\Psi = 10^6$ was used. The choice of scale factor will be dependent on the material properties and problem dimensions.

5 Conclusions

This research has highlighted some issues arising from the coupling of the BEM and SBFEM. The coupled BE-SBFEM has been developed for applications to linear elastic fracture mechanics, with the view to establishing an efficient method for modelling a crack tip region within a general domain. Restrictions in boundary conditions imposed in the earlier development of Chidgzey *et al.* [22] have been overcome in the present work. The BE-SBFEM has compared favourably with examples whose solutions are analytical in nature. Further, the BE-SBFEM has demonstrated geometric flexibility by modelling irregular domains with few degrees of freedom, and without the cumbersome substructuring requirements a SBFEM-only approach would make. A strategy has been hypothesised for determining with confidence the stress intensity factor of problems more typical of practical engineering applications. Following this strategy, stress intensity factor estimations have shown to offer good convergence. The condition number of the system matrix has been shown to be sensitive to the range of the orders of magnitude of terms in the BEM traction and displacement influence matrices. Ill-conditioning that may occur in examples of a real engineering nature may be reduced the use of an appropriate traction scale factor.

6 Acknowledgements

The first author acknowledges gratefully the financial support offered jointly by the Engineering and Physical Research Council (EPSRC) and the School of Engineering, Durham University.

References

[1] Deeks, A.J. and J.P. Wolf, *A virtual work derivation of the scaled boundary finite-element method for elastostatics.* Computational Mechanics, 2002. **28**(6): p. 489-504.

[2] Aliabadi, M.H., *A new generation of boundary element methods in fracture mechanics.* International Journal of Fracture, 1997. **86**(1-2): p. 91-125.

† http://www.mathworks.com/access/helpdesk/help/techdoc/ref/mldivide.html

[3] Moës, N., J. Dolbow, and T. Belytschko, *A finite element method for crack growth without remeshing.* International Journal for Numerical Methods in Engineering, 1999. **46**(1): p. 131-150.

[4] Wolf, J.P. and C. Song, *Dynamic-stiffness matrix in time domain of unbounded medium by infinitesimal finite element cell method.* Earthquake Engineering & Structural Dynamics, 1994. **23**(11): p. 1181-1198.

[5] Song, C. and J.P. Wolf, *Consistent infinitesimal finite-element cell method for diffusion equation in unbounded medium.* Computer Methods in Applied Mechanics and Engineering, 1996. **132**(3-4): p. 319-334.

[6] Wolf, J.P. and C. Song, *Finite-element modelling of unbounded media*. 1997: Wiley. 331.

[7] Song, C. and J.P. Wolf, *The scaled boundary finite-element method--alias consistent infinitesimal finite-element cell method--for elastodynamics.* Computer Methods in Applied Mechanics and Engineering, 1997. **147**(3-4): p. 329-355.

[8] Song, C. and J.P. Wolf, *Body loads in scaled boundary finite-element method.* Computer Methods in Applied Mechanics and Engineering, 1999. **180**(1-2): p. 117-135.

[9] Wolf, J.P. and C. Song, *The scaled boundary finite-element method - a primer: derivations.* Computers & Structures, 2000. **78**(1-3): p. 191-210.

[10] Song, C. and J.P. Wolf, *The scaled boundary finite-element method - a primer: solution procedures.* Computers & Structures, 2000. **78**(1-3): p. 211-225.

[11] Deeks, A.J. and J.P. Wolf, *Stress recovery and error estimation for the scaled boundary finite-element method.* International Journal for Numerical Methods in Engineering, 2002b. **54**(4): p. 557-583.

[12] Deeks, A.J. and J.P. Wolf, *An h-hierarchical adaptive procedure for the scaled boundary finite-element method.* International Journal for Numerical Methods in Engineering, 2002c. **54**(4): p. 585-605.

[13] Vu, T.H. and A.J. Deeks, *A p-adaptive scaled boundary finite element method based on maximization of the error decrease rate.* Computational Mechanics, 2008. **41**(441-455).

[14] Vu, T.H., *Enhancing the scaled boundary finite element method*, in *School of Civil & Resource Engineering*. 2006, University of Western Australia: Perth.

[15] Deeks, A.J., *Prescribed side-face displacements in the scaled boundary finite-element method.* Computers & Structures, 2004. **82**(15-16): p. 1153-1165.

[16] Chidgzey, S.R. and A.J. Deeks, *Determination of coefficients of crack tip asymptotic fields using the scaled boundary finite element method.* Engineering Fracture Mechanics, 2005. **72**(13): p. 2019-2036.

[17] Williams, E.W., *On the stress distribution at the base of a stationary crack.* Journal of Applied Mechanics, 1957. **24**: p. 109-114.

[18] Yang, Z., *Application of scaled boundary finite element method in static and dynamic fracture problems.* Acta Mechanica Sinica, 2006a. **22**(3): p. 243-256.

[19] Yang, Z., *Fully automatic modelling of mixed-mode crack propagation using scaled boundary finite element method.* Engineering Fracture Mechanics, 2006b. **73**(12): p. 1711-1731.

[20] Yang, Z.J. and A.J. Deeks. *A FEM-SBFEM coupled method for fully-automatic modelling of cohesive discrete crack propagation*. in *15th UK Conference of the Association of Computational Mechanics in Engineering*. 2007.

[21] Deeks, A.J. and C.E. Augarde, *A meshless local Petrov-Galerkin scaled boundary method.* Computational Mechanics, 2005. **V36**(3): p. 159-170.

[22] Chidgzey, S.R., J. Trevelyan, and A.J. Deeks, *Coupling of the boundary element method and the scaled boundary finite element method for computations in fracture mechanics.* Computers & Structures, 2008. **86**: p. 1198-1203.

[23] Trevelyan, J. and P. Wang, *Interactive re-analysis in mechanical design evolution. Part I. Background and implementation.* Computers & Structures, 2001a. **79**(9): p. 929-938.

[24] Trevelyan, J. and P. Wang, *Interactive re-analysis in mechanical design evolution. Part II. Rapid evaluation of boundary element integrals.* Computers & Structures, 2001b. **79**(9): p. 939-951.

[25] Becker, A.A., *The Boundary Element Method in Engineering*. 1992: McGraw-Hill International, London.

[26] Sladek, V. and J. Sladek, *The calculation of singular integrals in the boundary integral formulation of two-dimensional elastostatics.* Engineering Analysis, 1986. **3**(1): p. 25-35.

[27] Aliabadi, M.H. and D.P. Rooke, *Numerical Fracture Mechanics*, ed. G.M.L. Gladwell. 1992: Kluwer Academic Publishers/Computational Mechanics Publications.

[28] Aliabadi, M.H., *The boundary element method*. Vol. 2. 2002: Wiley.

[29] Aliabadi, M.H., *Database of Stress Intensity Factors*. 1996: Computational Mechanics Publications, Southampton.

[30] Portela, A., M.H. Aliabadi, and D.P. Rooke, *Dual boundary analysis of cracked plates: singularity subtraction technique.* International Journal of Fracture, 1992. **55**: p. 17-28.

[31] Civilek, M.B. and F. Erdogan, *Crack problems for a rectangular plate and an infinite strip.* International Journal of Fracture, 1982. **19**: p. 139-152.